Non-spherical bubble dynamics in a compressible liquid. Part 2. Acoustic standing wave

Wang, Qian; Blake, John

DOI:
10.1017/jfm.2011.149

J. Fluid Mech. (2011), *vol.* 679, *pp.* 559–581.
doi:10.1017/jfm.2011.149

Non-spherical bubble dynamics in a compressible liquid. Part 2. Acoustic standing wave

Q. X. WANG† AND J. R. BLAKE

School of Mathematics, the University of Birmingham, Birmingham B15 2TT, UK

(Received 26 April 2010; revised 25 February 2011; accepted 21 March 2011; first published online 24 May 2011)

This paper investigates the behaviour of a non-spherical cavitation bubble in an acoustic standing wave. The study has important applications to sonochemistry and in understanding features of therapeutic ultrasound in the megahertz range, extending our understanding of bubble behaviour in the highly nonlinear regime where jet and toroidal bubble formation may be important. The theory developed herein represents a further development of the material presented in Part 1 of this paper (Wang & Blake, *J. Fluid Mech.* vol. 659, 2010, pp. 191–224) to a standing wave, including repeated topological changes from a singly to a multiply connected bubble. The fluid mechanics is assumed to be compressible potential flow. Matched asymptotic expansions for an inner and outer flow are performed to second order in terms of a small parameter, the bubble-wall Mach number, leading to weakly compressible flow formulation of the problem. The method allows the development of a computational model for non-spherical bubbles by using a modified boundary-integral method. The computations show that the bubble remains approximately of a spherical shape when the acoustic pressure is small or is initiated at the node or antinode of the acoustic pressure field. When initiated between the node and antinode at higher acoustic pressures, the bubble loses its spherical shape at the end of the collapse phase after only a few oscillations. A high-speed liquid bubble jet forms and is directed towards the node, impacting the opposite bubble surface and penetrating through the bubble to form a toroidal bubble. The bubble first rebounds in a toroidal form but re-combines to a singly connected bubble, expanding continuously and gradually returning to a near spherical shape. These processes are repeated in the next oscillation.

Key words: bubble dynamics, cavitation, sonoluminescence

1. Introduction

In Wang & Blake (2010, hereafter referred to as Part 1), we developed a weakly compressible theory for non-spherical bubble dynamics when subjected to a harmonic acoustic travelling wave. In this paper, we carry out a similar study using matched asymptotic perturbations for non-spherical bubble dynamics in a standing wave but include new developments by (i) considering a general plane wave and (ii) modelling multiple topological changes of the bubble. A standing wave often occurs in a

† Email address for correspondence: wangqx@maths.bham.ac.uk

cavitation environment due to the superposition of a plane wave and the reflected wave from a rigid wall.

The study has important applications to sonochemistry and in understanding features of therapeutic ultrasound in the megahertz range, where jet and toroidal bubble formation may be important (Lauterborn & Kurz 2010). In sonochemistry, acoustically driven cavitation is used to promote mixing and reactions (Dahnke, Swamy & Keil 1999). Reaction sites can often be observed as luminescing bubbles line up across the antinode of a standing wave (Crum & Cordry 1994) with the internal gas temperatures and chemical composition of importance in determining the reactions that can take place. In aqueous systems, acoustic cavitation is used in ultrasonic cleaners and processors, environmental remediation or enhanced crystallization (Leighton 1994; Brennen 1995; Blake *et al.* 1999). Acoustic cavitation plays a key role in numerous medical procedures, including sonoporation and ultrasound lithotripsy (Goldberg *et al.* 1994; Putterman & Weninger 2000; Day 2005; Klaseboer *et al.* 2007; Calvisi, Iloreta & Szeri 2008).

This paper concerns the behaviour of a micro-bubble (5–100 μm) in an acoustic standing wave. As noted in Part 1, the behaviour is controlled by a range of physical phenomena: the amplitude of the acoustic pressure, bubble size, bubble concentration (distance to nearest neighbour), gas solubility, heat transfer, surface tension and, for micro-bubbles, viscosity, may have an influence over part of the cycle, but is typically dominated by inertial effects, with Reynolds number of (10^2–10^4). The weak compressibility of the liquid should be considered for describing the acoustic wave and to facilitate the dispersive radiation of energy (Prosperetti & Lezzi 1986; Wang & Blake 2010). Acoustic bubbles may also be associated with a violent collapse, where compressibility needs to be incorporated to yield a more realistic and practical model (Brenner, Hilgenfeldt & Lohse 2002).

A spherical bubble in a compressible fluid was first considered in connection with an underwater explosion (Herring 1941; Cole 1948). The acoustic radiation into the liquid from the oscillating bubble has been integrated into the Rayleigh model for spherical bubbles by Gilmore (1952) and Keller and his collaborators (Keller & Kolodner 1956; Epstein & Keller 1971; Keller & Miksis 1980). It has been widely used in the study of acoustic bubbles in a plane standing wave and sonoluminescence (Prosperetti, Crum & Commander 1988; Kamath, Prosperetti & Egolfopoulos 1993; Brenner, Lohse & Dupont 1995; Matula *et al.* 1997; Hilgenfeldt *et al.* 1998; Brenner *et al.* 2002). Prosperetti & Lezzi (1986) and Lezzi & Prosperetti (1987) studied the radial dynamics of spherical bubbles in compressible fluids using matched asymptotic expansions in terms of the bubble-wall Mach number. The theoretical studies of a bubble in a standing wave have been largely based on the assumption that the bubble is approximately spherical (Feng & Leal 1997). The translation of a bubble is driven by a 'Bjerknes force' generated by a pressure gradient (Eller 1968; Brennen 1995).

Earlier studies considered the heat and mass transfer during the violent collapse of non-spherical bubbles, showing in particular how the non-sphericity, including the high-speed liquid jet and toroidal bubble formulation, can lead to significantly lower gas temperatures (Calvisi *et al.* 2007). These collapse characteristics and resulting flow field are important to sonochemistry as peak temperatures, strain rates, pressures, mixing and radical production are affected. Modelling the internal chemistry and thermodynamics is complicated depending on a range of parameters (e.g. evaporation, condensation, molar fraction of species in mixture, water density, mass density and gas constant of mixture). The physics will involve thermal and compositional boundary

layers in both liquid and gas. A major theoretical approximation is to regard the thermodynamics as slow or rapid. In the slow mode, temperature and chemical composition within the bubble are assumed uniform, with water vapour freely entering the bubble with minimal change in surface temperature. In the fast mode, the bubble motion is much faster so that mass and thermal transfer may be neglected. Models that have incorporated the concept of both slow and rapid thermodynamics have used a changeover time as the equilibrium bubble radius in some therapeutic ultrasound studies (Coussis & Roy 2008), while others have used a more detailed thermodynamics behaviour to obtain the changeover time (see e.g. Szeri *et al.* 2003). However, in this paper, we will consider just two cases, solely adiabatic and solely isothermal with the algorithmic approximations mentioned above lying between the two extremes.

Viscous effects may be important for very small bubbles, especially during 'after-bounce' behaviour associated with the natural frequency of a bubble which is most noticeable when the driving frequency is much lower than the natural frequency, as might occur in single-bubble sonoluminescence (SBSL), see also figure 2. In the case of spherical bubbles, viscosity only enters the analysis through the normal stress on the surface of the bubble but plays no role in the fluid body, apart from viscous dissipation. Physically, this is realized in the extra work required to expand the bubble against this additional normal viscous force on the bubble surface (see e.g. Gilmore 1952). If two modes of motion were included for the bubble (i.e. radial motion and translational motion), a further viscous drag term would enter the global momentum equation for the translational mode, thus dissipating energy associated with the Kelvin impulse or Bjerknes force due to the spatially dependent wave form (as in a travelling or a standing wave). Some authors include the normal viscous force in non-spherical bubble models (through the $2\mu(\partial^2/\varphi\partial n^2)$ term in Miksis, Vanden-Broeck & Keller 1982) but note the failure of this method to incorporate the pressure drop associated with the boundary layers, particularly at the poles of the bubble (Moore 1963). Boulton-Stone & Blake (1993) developed a viscous boundary layer approach around a bursting bubble by exploiting the properties for a normal filament remaining perpendicular to a stress-free surface (Batchelor 1968). Their analysis showed that the addition of a boundary layer to this inertially dominant flow only marginally slowed the liquid jet. Higher-order modes, often associated with parametric excitation, are also damped by viscous effects and will generate heat in a thin layer of the surrounding liquid (Prosperetti 1977; Popinet & Zaleski 2002; Versluis *et al.* 2010). The principal objective of this paper though is to show the effects of compressibility on bubble motion so we will not include viscous effects in our analysis but instead note that viscous effects will lead to greater work done during volume change as well as slowing the translational motion which may even completely impede jet formation for low enough Reynolds numbers ($R_e < 25$) (Popinet & Zaleski 2002).

Bubble dynamics in a compressible liquid may also be simulated using domain approaches coupled with various interface-capturing schemes (Hua & Lou 2007; Yue *et al.* 2007; Johnsen & Colonius 2008, 2009; Turangan *et al.* 2008). Johnsen & Colonius (2008, 2009) analysed the dynamics of the shock-induced and Rayleigh collapse of a bubble near a planar rigid surface and in a free field using the unsteady Euler equations based on an inviscid and compressible flow model. Domain simulation of this multi-scaled problem of multiple oscillations (as many as 20 cycles or more) is computationally demanding, even if feasible on multiprocessor machines. The theoretical developments in this paper however provide greater insight into the physical process, (e.g. input wave, acoustic radiation, Bjerknes' force and the Kelvin impulse), as well as reducing the computational complexity.

This paper is organized as follows. In § 2, the flow problem is formulated based on compressible potential flow theory. The asymptotic analyses of the inner and outer flows is briefly described in § 3 and are summarized in § 4. In § 5, the numerical model using the mixed-Eulerian–Lagrangian (MEL) modelling is formulated and developed for a bubble in a standing wave to include repeated topological change from singly to multiply connected. In §§ 6 and 7, the calculation is performed for the case with low and high acoustic pressures, respectively. The summary and conclusions are presented in § 8.

2. Mathematical formulation

Consider a cavitation bubble with typical radius of $O(\mu\text{m–mm})$ in an acoustic wave due to high frequency ultrasound $O(10^2\text{–}10^3)\,\text{kHz}$ at differing intensities in the range $O(10^1\text{–}10^3)\,\text{W cm}^{-2}$ (cf. Young 1989; Leighton 1994; Brennen 1995; Blake *et al.* 1999). In this situation, the bubble dynamics can be modelled approximately based on potential flow theory. We assume that the bubble radius is small compared to the wavelength of the acoustic wave. The wavelength λ of an acoustic wave is $\lambda = c/f \geqslant 10\,\text{mm}$, when the acoustic frequency $f \leqslant 150\,\text{kHz}$, where c is the sound speed in water ($c = 1500\,\text{m s}^{-1}$).

The reference length R_s is chosen as the equilibrium radius of the bubble, the reference density ρ_∞ is the density in the undisturbed liquid, and the reference pressure p_∞ is the pressure in the undisturbed liquid, often taken to be atmospheric pressure. We use the reference velocity $U = \sqrt{p_\infty/\rho_\infty}$, as the driving pressure is normally measured as fractions or multiplies of atmospheric pressure. For reference purpose, U takes the value of $10\,\text{m s}^{-1}$ in water at atmospheric pressure. We thus introduce the following non-dimensional quantities, indicated by asterisks:

$$\boldsymbol{r} = R_s \boldsymbol{r}_*, \quad t = \frac{R_s}{U} t_*, \quad \varphi = R_s U \varphi_*, \quad c = c_\infty c_*, \quad p = p_\infty (1 + p_*). \tag{2.1a–e}$$

Here φ is the velocity potential. The sound speed c is normalized by its value at the undisturbed liquid c_∞. In the following discussion we refer to dimensionless quantities unless specified otherwise.

A Cartesian coordinate system is chosen, with the origin at the centre of the bubble at $t_* = 0$, and the z_*-axis is along the direction of the acoustic wave. The liquid flow is governed by the equation of mass conservation

$$\nabla_*^2 \varphi_* + \frac{\varepsilon^2}{c_*^2} \left(\frac{\partial h_*}{\partial t_*} + \nabla_* \varphi_* \cdot \nabla_* h_* \right) = 0, \tag{2.2a}$$

and the Bernoulli equation,

$$\frac{\partial \varphi_*}{\partial t_*} + \frac{1}{2} |\nabla_* \varphi_*|^2 + h_* = 0. \tag{2.2b}$$

Here the parameter

$$\varepsilon = \frac{U}{c_\infty} \tag{2.3}$$

is the bubble-wall Mach number, which is assumed to be small in the present study. This theory is thus valid for weakly compressible fluids, where the nonlinear shock-wave formulation has a negligible effect on the flow. The small parameter ε can also be interpreted as the ratio of the typical scale of the bubble radius R_s over the wavelength λ of the acoustic wave (Wang & Blake 2010).

We assume that thermal effects in the liquid itself are insignificant. The liquid state is thus completely defined by a single thermodynamic variable. The sound speed c_* and enthalpy h_* of the liquid can be given approximately as follows (Wang & Blake 2010, (2.8*a*,*b*) therein):

$$c_*^2 = 1 + \varepsilon^2(n-1)h_*, \tag{2.4a}$$

$$h_* = p_* - \tfrac{1}{2}\varepsilon^2 p_*^2 + o(\varepsilon^2). \tag{2.4b}$$

Substituting (2.4) into (2.2) yields

$$\nabla_*^2\varphi_* + \frac{\varepsilon^2}{c_*^2}\left(\frac{\partial p_*}{\partial t_*} + \nabla_*\varphi_*\cdot\nabla_* p_*\right) = O(\varepsilon^4), \tag{2.5a}$$

$$\frac{\partial\varphi_*}{\partial t_*} + \frac{1}{2}|\nabla_*\varphi_*|^2 + p_* = O(\varepsilon^2). \tag{2.5b}$$

The present modelling is formulated directly in terms of pressure of the liquid rather than on enthalpy as in Part 1.

The kinematic material boundary condition on the bubble surface S is

$$\frac{\mathrm{d}r_*}{\mathrm{d}t_*} = \nabla_*\varphi_*. \tag{2.6}$$

Assuming that the expansion and contraction of the bubble gas is adiabatic, the liquid pressure p_L on the bubble surface is given by,

$$p_{L*} = p_{v*} + p_{g0*}\left(\frac{V_{0*}}{V_*}\right)^{\gamma} - \sigma_*\left(\frac{1}{R_{1*}} + \frac{1}{R_{2*}}\right), \tag{2.7}$$

where p_{v*} is the partial pressure of vapour of the bubble, $p_{g0*} = p_{g0}/p_\infty$ is the equilibrium partial pressure of the non-condensable gas content of the bubble, V_* is the bubble volume and V_{0*} is its initial value, and γ is the ratio of the specific heats of the gas content, R_{1*} and R_{2*} are the principal radii of curvature and $\sigma_* = \sigma/(R_s P_\infty)$ is the surface tension coefficient.

Assuming the acoustic wave to be a plane propagating wave along the z_*-axis yields the condition at infinity of

$$\varphi|_{r_*\to\infty} = \varphi_{a*} = f_*(\omega_* t_* - k_* z_*) + g_*(\omega_* t_* + k_* z_*), \tag{2.8}$$

where the wavenumber k_* and frequency ω_* of the acoustic wave can be obtained from their corresponding dimensional values k and ω, respectively, $k_* = R_s k$ and $\omega_* = R_s\omega/U$.

3. Matched asymptotic expansion

In Part 1, we developed a matched asymptotic expansions approach for a singly connected bubble subjected to a harmonic plane wave. This approach will be generalized for a doubly connected bubble subjected to a general plane wave. We will mainly focus on the differences between this paper and the earlier paper in the series (Wang & Blake 2010).

The inner region near the bubble where $(x, y, z) = O(R_s)$ and the outer region far away from the bubble where $(x, y, z) = O(\lambda)$, are illustrated in figure 1. The inner expansions for the potential φ_* and pressure p_* are as follows:

$$\varphi_*(\boldsymbol{r}_*, t_*) = \varphi_0(\boldsymbol{r}_*, t_*) + \varepsilon\varphi_1(\boldsymbol{r}_*, t_*) + \cdots, \tag{3.1a}$$

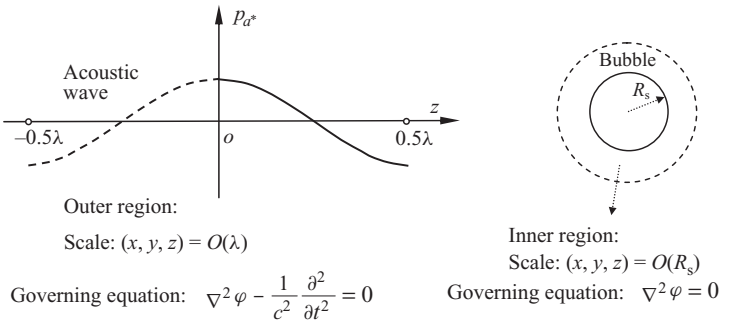

FIGURE 1. A representation of the weakly compressible model for a micro-cavitation bubble subjected to a plane standing wave, with the wavelength λ being much larger than the equilibrium radius of the bubble R_s.

$$p_*(\boldsymbol{r}_*, t_*) = p_0(\boldsymbol{r}_*, t_*) + \varepsilon p_1(\boldsymbol{r}_*, t_*) + \cdots. \tag{3.1b}$$

Substitution of (3.1) into (2.5*a*,*b*) yields the inner field equations,

$$\nabla_*^2\varphi_i = 0 \quad \text{for } i = 0, 1. \tag{3.2}$$

The general solutions of Laplace's equation (3.2) are given as follows:

$$\varphi_i(\boldsymbol{r}_*, t_*) = f_i(t_*) + g_i(t_*)z_* + \int_S \left(\frac{\partial \varphi_i(\boldsymbol{q}, t_*)}{\partial n} G(\boldsymbol{r}_*, \boldsymbol{q}) - \varphi_i(\boldsymbol{q}, t_*) \frac{\partial G(\boldsymbol{r}_*, \boldsymbol{q})}{\partial n} \right) \mathrm{d}S(\boldsymbol{q}) - \int_C \varphi_i(\boldsymbol{q}, t_*) \frac{\partial G(\boldsymbol{r}_*, \boldsymbol{q})}{\partial n} \mathrm{d}S(\boldsymbol{q}) \quad \text{for } i = 0, 1, \tag{3.3}$$

where the unknown functions $f_i(t_*)$, $g_i(t_*)$ for $i = 0, 1$ are to be determined by the matching between the inner and outer expansions, S is the bubble surface, $\boldsymbol{n}$ is the unit outward normal on the surface, $\boldsymbol{q}$ is the integration variable on the bubble surface S, and the free-space Green's function is

$$G(\boldsymbol{r}_*, \boldsymbol{q}) = \frac{1}{4\pi} \frac{1}{|\boldsymbol{r}_* - \boldsymbol{q}|}. \tag{3.4}$$

The integral on the cut C in (3.3) is added only for a toroidal bubble, when the liquid field is doubly connected. The branch cut C across the jet is used to render the fluid domain singly connected (Best 1993).

The outer limit of the two lowest-order inner solutions is as follows:

$$(\varphi_*)^o = (\varphi_0)^o + \varepsilon(\varphi_1)^o = f_0(t_*) + g_0(t_*)z_* + \frac{1}{4\pi}\frac{m_0(t_*)}{r_*} + \varepsilon f_1(t_*) + \varepsilon g_1(t_*)z_* + O(\varepsilon^2), \tag{3.5}$$

where

$$m_0(t_*) = \int_S \frac{\partial \varphi_0(\boldsymbol{q}, t_*)}{\partial n} \mathrm{d}S(\boldsymbol{q}). \tag{3.6}$$

Denoting the outer expansions in terms of the outer variable $\tilde{\boldsymbol{r}} = \varepsilon \boldsymbol{r}_*$ as follows:

$$\varphi_* = \phi_0(\tilde{\boldsymbol{r}}, t_*) + \varepsilon\phi_1(\tilde{\boldsymbol{r}}, t_*) + \cdots, \tag{3.7a}$$

$$p_* = P_0(\tilde{\boldsymbol{r}}, t_*) + \varepsilon P_1(\tilde{\boldsymbol{r}}, t_*) + \cdots. \tag{3.7b}$$

Substituting (3.7) into (2.5*a*,*b*) yields the equations for the two lowest-order outer solutions

$$\tilde{\nabla}^2\phi_i - \frac{\partial^2\phi_i}{\partial t_*^2} = 0 \quad \text{for } i = 0,\ 1, \tag{3.8}$$

where the operator $\tilde{\nabla}$ is defined in terms of $\tilde{\boldsymbol{r}}$.

The leading outer solution is the incident acoustic wave

$$\phi_0 = f_*(\omega_*(t_* - \tilde{z})) + g_*(\omega_*(t_* + \tilde{z})). \tag{3.9}$$

The general solution of the second-order outer solution ϕ_1 can be obtained as follows:

$$\phi_1 = \frac{F_1(t_* - \tilde{r})}{\tilde{r}}, \tag{3.10}$$

where F_1 is an arbitrary function having a second-order derivative.

The inner limits of the two lowest-order outer expansions (3.9) and (3.10) can be obtained as follows:

$$(\phi)^i = f_*(\omega_* t_*) + g_*(\omega_* t_*) + \varepsilon\omega_* z_*(-f_*'(\omega_* t_*) + g_*'(\omega_* t_*)) + \frac{F_1(t_*)}{r_*} - \varepsilon F_1'(t_*) + O(\varepsilon^2). \tag{3.11}$$

Using Van Dyke's matching principle (Van Dyke 1975) with (3.5) and (3.11) yields

$$f_0(t_*) = f_*(\omega_* t_*) + g_*(\omega_* t_*), \quad g_0(t_*) = 0, \tag{3.12a}$$

$$F_1(t_*) = \frac{m_0(t_*)}{4\pi}, \tag{3.12b}$$

$$f_1(t_*) = -F_1'(t_*) = -\frac{m_0'(t_*)}{4\pi}, \quad g_1(t_*) = \omega_*(-f_*'(\omega_* t_*) + g_*'(\omega_* t_*)). \tag{3.12c}$$

Combining (3.9), (3.10), (3.12*c*) yields the first two outer solution terms,

$$\phi = f_*(\omega_*(t_* - \tilde{z})) + g_*(\omega_*(t_* + \tilde{z})) + \varepsilon\frac{m_0(t_* - \tilde{r})}{4\pi\tilde{r}} + O(\varepsilon^2). \tag{3.13}$$

The outer flow becomes a direct problem to second order. The first-order outer solution is the incident acoustic wave, and the second-order outer solution is due to a point source whose strength is equal to the rate of change of the bubble volume.

4. The theoretical basis for the computational model: second-order theory

The combined two lowest-order inner solutions, $\varphi_*(\boldsymbol{r}_*, t_*) = \varphi_0(\boldsymbol{r}_*, t_*) + \varepsilon\varphi_1(\boldsymbol{r}_*, t_*)$, yield the following set of equations for the potential,

$$\nabla_*^2\varphi_* = O(\varepsilon^2), \tag{4.1a}$$

$$\frac{\mathrm{d}\boldsymbol{r}_*}{\mathrm{d}t_*} = \nabla_*\varphi_* + O(\varepsilon^2) \quad \text{on } S, \tag{4.1b}$$

$$\frac{\partial\varphi_*}{\partial t_*} + \frac{1}{2}|\nabla_*\varphi_*|^2 + p_{L*} = O(\varepsilon^2) \quad \text{on } S, \tag{4.1c}$$

$$\varphi_*|_{r_*\to\infty} = f_0(t_*) + \varepsilon f_1(t_*) + \varepsilon g_1(t_*)z_* + \frac{1}{4\pi}\frac{m_0(t_*)}{r_*} + O(\varepsilon^2). \tag{4.1d}$$

One can draw the following conclusion from (4.1): to second order (first order in ε) the problem reduces to Laplace's equation with the compressible effects appearing

only in the far-field condition (4.1*d*). We know from (4.1*d*) that the fluid velocity in the far field is $\nabla_*\varphi_*|_{r_*\to\infty} = \varepsilon g_1(t_*)\boldsymbol{k}$, where $\boldsymbol{k}$ is the unit vector along the z_*-axis.

Assuming that the bubble is in an equilibrium state before the arrival of the acoustic wave, the initial condition on the bubble surface is given by

$$\varphi_{n*}|_{t_*=0} = \varepsilon g_1(0)\boldsymbol{n}\cdot\boldsymbol{k} \quad \text{on } r_* = R_{0*}. \tag{4.2}$$

We choose the coordinates $\boldsymbol{r}_b$ moving with a (time-dependent) uniform stream at infinity, in which the flow velocity vanishes at infinity

$$t_b = t_*, \quad \boldsymbol{r}_b = \boldsymbol{r}_* + \varepsilon(f_*(\omega_* t_*) - g_*(\omega_* t_*))\boldsymbol{k}. \tag{4.3}$$

In addition, we make the following decomposition:

$$\varphi_* = f_0(t_b) + \varepsilon f_1(t_b) + \varepsilon g_1(t_b) z_b + \Phi. \tag{4.4}$$

Substituting (4.3), (4.4) into (4.1) yields

$$\nabla_b^2\Phi = O(\varepsilon^2), \tag{4.5a}$$

$$\frac{\mathrm{d}\boldsymbol{r}_b}{\mathrm{d}t_b} = \nabla_b\Phi + O(\varepsilon^2) \quad \text{on } S, \tag{4.5b}$$

$$\frac{\mathrm{d}\Phi}{\mathrm{d}t_b} = 1 + \frac{1}{2}|\nabla_b\Phi|^2 - \left(p_{v*} + p_{g0*}\left(\frac{V_{0*}}{V_*}\right)^{\gamma} - \sigma_*\left(\frac{1}{R_{1*}} + \frac{1}{R_{2*}}\right)\right)$$
$$-\omega_*(f_*'(\omega_* t_b) + g_*'(\omega_* t_b)) + \varepsilon\frac{1}{4\pi}m_0''(t_b) + \varepsilon\omega_*^2(f_*''(\omega_* t_b) - g_*''(\omega_* t_b))z_b + O(\varepsilon^2), \tag{4.5c}$$

$$\Phi|_{r_b\to\infty} = \frac{1}{4\pi}\frac{m_0(t_b)}{r_b} + O(\varepsilon^2), \tag{4.5d}$$

$$\Phi_{n*}|_{t_b=0} = 0 \quad \text{on } r_* = R_{0*}. \tag{4.5e}$$

Note (3.12) has been used in deriving (4.5*c*).

Using the definition $m_o(t_*)$ in (3.6) and (4.4) leads to

$$m_0(t_b) = \int_S \frac{\partial\Phi}{\partial n}\mathrm{d}S + O(\varepsilon). \tag{4.6}$$

Like in the special case of a harmonic progressive wave (Wang & Blake 2010), there are three additional terms associated with the acoustic wave contribution in the dynamic condition on the bubble surface (4.5*c*). The first term of $O(1)$, $-\omega_*(f_*'(\omega_* t_b) + g_*'(\omega_* t_b))$, represents the local acoustic pressure at the bubble centre:

$$p_{a*}(t_b) = -\left.\frac{\partial\varphi_{a*}}{\partial t_b}\right|_{z_*=0} = -\omega_*(f_*'(\omega_* t_b) + g_*'(\omega_* t_b)). \tag{4.7}$$

The second term, $\varepsilon(1/4\pi)m_0''(t_b)$, is associated with an outward-propagating acoustic wave due to the bubble's oscillations. The first two terms yield only spherical wave field effects.

However, the third term, $\varepsilon\omega_*^2(f_*''(\omega_* t_b) - g_*''(\omega_* t_b))z_b$, is associated with the inertial force effect due to the acoustic wave and breaks the spherical symmetry. Using (4.3), the acceleration of the system $\boldsymbol{r}_b$ can be calculated as

$$\boldsymbol{a}_{b*} = \varepsilon\omega_*^2(-f_*''(\omega_* t_b) + g_*''(\omega_* t_b))\boldsymbol{k}. \tag{4.8a}$$

The inertial force on the bubble is given by

$$\boldsymbol{F}_{I*} = V_*\varepsilon\omega_*^2(f_*''(\omega_* t_b) - g_*''(\omega_* t_b))\boldsymbol{k}. \tag{4.8b}$$

The inertial force is equivalent to the more well-known Bjerknes force acting on the bubble, which is the resultant force due to the pressure gradient acting over the bubble surface. To calculate the Bjerknes force using the Gauss's divergence theorem, we extend $p_{a*}(\boldsymbol{r}_*, t_b)$ into the inner region continuously using the same expression of the function. The Bjerknes force may be obtained as follows:

$$\boldsymbol{F}_{B*} = -\oint_S p_{a*}\boldsymbol{n}_b \,\mathrm{d}S = -\omega_* \oint_S (f'_*(\omega_* t_b - \varepsilon\omega_* z_b) + g'_*(\omega_* t_b + \varepsilon\omega_* z_b))\boldsymbol{n}_b \,\mathrm{d}S, \tag{4.9}$$

where $\boldsymbol{n}_b$ is the outer normal to the inner region of the bubble. The force can be simplified by using a Taylor expansion and the Gauss's divergence theorem to the inner region of the bubble as follows:

$$\begin{aligned}\boldsymbol{F}_{B*} &= -\omega_* \oint_S [f'_*(\omega_* t_b) + g'_*(\omega_* t_b) + (-f''_*(\omega_* t_b) + g''_*(\omega_* t_b))\varepsilon\omega_* z_b + O(\varepsilon^2)]\boldsymbol{n} \,\mathrm{d}S \\ &= -\varepsilon\omega_*^2 \int_V (f''_*(\omega_* t_b) - g''_*(\omega_* t_b)) \,\mathrm{d}V \boldsymbol{k} = -V_*\varepsilon\omega_*^2 (f''_*(\omega_* t_b) - g''_*(\omega_* t_b))\boldsymbol{k}. \end{aligned} \tag{4.10}$$

The Bjerknes force is equal in magnitude but opposite in direction to the inertial force (4.8*b*) acting on the bubble. The Bjerknes force is therefore proportional to the square of the frequency of the acoustic wave. In the case of a standing wave,

$$f_* = \tfrac{1}{2} b_* \cos(\omega_* t_* - k_* z_* - \theta_0), \quad g_* = \tfrac{1}{2} b_* \cos(\omega_* t_* + k_* z_* + \theta_0), \tag{4.11}$$

where b_* and θ_0 are respectively the amplitude and initial phase of the acoustic standing wave, given the initial location of the bubble is at $z_* = 0$. Substituting into (4.5*c*) yields

$$\begin{aligned}\frac{\mathrm{d}\Phi}{\mathrm{d}t_b} &= \frac{1}{2}|\nabla_b \Phi|^2 - \left(p_{v*} + p_{g0*}\left(\frac{V_{0*}}{V_*}\right)^{\gamma} - \sigma_*\left(\frac{1}{R_{1*}} + \frac{1}{R_{2*}}\right)\right) + b_*\omega_* \cos(\theta_0)\sin(\omega_* t_b) \\ &\quad + \varepsilon\frac{1}{4\pi}\mathrm{m}''_0(t_b) - \varepsilon b_*\omega_*^2 \sin(\theta_0)\sin(\omega_* t_b) z_b + O(\varepsilon^2). \end{aligned} \tag{4.12}$$

The first-order local acoustic pressure at the centre of the bubble given by (4.7) is

$$p_{a*}(t_*) = a_* \cos(\theta_0)\sin(\omega_* t_*), \tag{4.13}$$

where $p_a(t_b) = p_\infty p_{a*}(t_b)$, $a_* = b_*\omega_*$. Note that $\theta_0 = 0$ corresponds to an antinode, and $\theta_0 = \pi/2$ a node, in the standing wave.

There is an antisymmetric property for a bubble motion in a standing wave. By examining the governing equations of (4.5*a*,*b*,*d*,*e*) and (4.12) for Φ, we note that if $\Phi(x_b, y_b, z_b, t, \theta_0)$ satisfies the governing equations then $\Phi(x_b, y_b, -z_b, t, -\theta_0)$ also satisfies the governing equations. Thus, the motion of the bubble is antisymmetric in the region $\theta_0 \in [-\pi, \pi]$ so our calculations will be carried out only for $\theta_0 \in [0, \pi]$.

5. Numerical modelling using the mixed-Eulerian–Lagrangian method

The initial boundary-value problem defined by (4.5*a*, *b*, *d*, *e*) and (4.12) can be solved numerically using a boundary-integral method coupled with an MEL method. The numerical model for a singly connected bubble can be found in Blake, Taib & Doherty (1986), Wang *et al.* (1996*a*) and Part 1. However, this section will focus on the modelling of toroidal bubbles.

5.1. *Vortex ring model for toroidal bubbles*

Under an asymmetric environment, a high-speed liquid jet often forms during bubble collapse and subsequently impacts the opposite bubble surface. Once jet impact has occurred, the liquid domain is transformed from a singly connected to a doubly connected form. A circulation is generated around the toroidal bubble since a potential jump occurs at the impact point. Several approaches have been developed to model the transition from a singly to a doubly connected domain. Best (1993) modelled this transition to a toroidal bubble, by introducing a domain cut to render the liquid domain singly connected. Zhang, Duncan & Chahine (1993) and Zhang & Duncan (1994) have modelled this circulation by introducing a vortex sheet that moves with the fluid.

Pedley (1968) developed a theoretical model for a toroidal bubble with a vortex ring inside the bubble to account for the circulation. Later, Lundgren & Mansour (1991) modelled a toroidal bubble initiated as a bubble ring with circular cross-section with a vortex ring inside the bubble and a dipole distribution to the bubble surface. Wang *et al.* (1996*b*, 2005) developed these earlier ideas to model the topological transition of a bubble and the subsequent toroidal bubble, by placing a vortex ring inside the toroidal bubble.

The strength of the vortex ring is the circulation Γ of the flow along a closed path that threads through the torus, which is equal to the jump of the potential ϕ across the contact points at the time of impact. Thus,

$$\Gamma = \oint_C \nabla_* \varphi_* \cdot \mathrm{d}\boldsymbol{r} = \varphi_{*N+1} - \varphi_{*1}, \tag{5.1}$$

where φ_{*1} and φ_{*N+1} are potentials at the impact point. For an incompressible potential flow, the circulation Γ is invariant in time.

The potential is now decomposed into two parts: the potential of the vortex ring ϕ_{vr} and a remnant potential ϕ as follows:

$$\varphi_* (\boldsymbol{r}_*, t_*) = f_0 (t_b) + \varepsilon f_1 (t_b) + \varepsilon g_1 (t_b) z_b + \phi_{vr} (\boldsymbol{r}_*) + \phi (\boldsymbol{r}_*, t_*) . \tag{5.2}$$

Here we have also included the term $f_0 (t_b) + \varepsilon f_1 (t_b) + \varepsilon g_1 (t_b) z_b$ as we did for (4.4). With the potential jump being accounted by the vortex ring using (5.1), the remnant potential ϕ_* is continuous in the flow field.

The velocity of the vortex ring $\boldsymbol{v}_{vr}$ can be obtained analytically using the Biot–Savart law (Wang *et al.* 1996*b*). The velocity potential due to the vortex ring is further obtained by the line integral of the velocity from the far field, to let the potential of the vortex ring vanish at infinity. The potential of the vortex ring thus satisfies Laplace's equation in the fluid domain and vanishes at infinity.

Substituting (4.3) and (5.2) into (4.1*a*,*b*,*d*) and (4.12) yields the boundary-value problem for the remnant potential ϕ as follows:

$$\nabla_b^2 \phi = O(\varepsilon^2), \tag{5.3a}$$

$$\frac{\mathrm{d}\boldsymbol{r}_b}{\mathrm{d}t_b} = \boldsymbol{v}_{vr} + \nabla_* \phi + O(\varepsilon^2) \quad \text{on } S, \tag{5.3b}$$

$$\frac{\mathrm{d}}{\mathrm{d}t_b}\left(\phi - \varepsilon \frac{1}{4\pi} m_0'(t_b)\right) = 1 - \boldsymbol{v}_{vr} \cdot (\boldsymbol{v}_{vr} + \nabla_b \phi) + \frac{1}{2}|\boldsymbol{v}_{vr} + \nabla_b \phi|^2 - p_{g0*}\left(\frac{V_{0*}}{V_*}\right)^{\gamma} + b_* \omega_* \cos(\theta_0) \sin(\omega_* t_b) - \varepsilon b_* \omega_*^2 \sin(\theta_0) \sin(\omega_* t_b) z_b + O(\varepsilon^2), \tag{5.3c}$$

$$\Phi|_{r_b\to\infty} = \frac{1}{4\pi}\frac{m_0(t_b)}{r_b} + O(\varepsilon^2), \tag{5.3d}$$

where $\boldsymbol{v}_{vr} = \nabla_b \phi_{vr}$ is the induced velocity due to the vortex ring.

The above governing equations for the remnant potential ϕ are in the same form as those for Φ given in (4.1*a*,*b*,*d*) and (4.12). Therefore, the remnant potential ϕ can be solved using the boundary-integral method and updated in time in the same manner as that for Φ of the simply connected pre-toroidal bubble.

For an axisymmetric case, the vortex ring is a circle with centre at the symmetry axis. In theory, the precise placement or location of the vortex ring (or loop) is immaterial so long as it lies completely within the toroidal bubble. In practice, to avoid possible numerical instability, the vortex ring should not be too close to the bubble surface. The location of the vortex ring, in the coordinate plane $\theta = 0$, (r_{vr}, z_{vr}), is chosen as follows:

$$z_{vr} = \frac{z_{min} + z_{max}}{2}, \quad r_{vr} = \frac{r_{c1} + r_{c2}}{2}, \tag{5.4}$$

where z_{min} and z_{max} are the minimum and maximum values of the z-coordinates of all the grids on the bubble surface; r_{c1} and r_{c2} are the r-coordinates of the two intersections of the horizontal line $z = z_{vr}$ and the curve C (the intersection of the coordinate plane $\theta = 0$ and the bubble surface).

This choice of the vortex ring location is more robust than the geometrical centroid used in the previous work (Wang *et al.* 1996*b*). However, as the bubble evolves and translates, the bubble surface may become too close to the vortex ring, resulting in numerical instability. To avoid this instability, the vortex ring is relocated using (5.4) when its minimum distance to the bubble surface is less than $0.05R_{eq*}$, where R_{eq*} is the equivalent bubble radius $R_{eq*} = (3/4\pi)V_*^{1/3}$. When the relocation is performed, we first use (5.2) to find the total potential

$$\varphi_*(\boldsymbol{r}_*, t_*) = f_0(t_b) + \varepsilon f_1(t_b) + \varepsilon g_1(t_b) z_b + \phi_{vr}^{old}(\boldsymbol{r}_*) + \phi^{old}(\boldsymbol{r}_*, t_*), \tag{5.5}$$

where $\phi_{vr}^{old}(\boldsymbol{r}_*)$ and $\phi^{old}(\boldsymbol{r}_*, t_*)$ are the potentials due to the vortex ring and the remnant potential before relocation. Since the total potential remains unchanged after the relocation of the vortex ring, the following equation can be used to find the remnant potential $\phi^{new}(\boldsymbol{r}_*, t_*)$ after the relocation:

$$\varphi_*(\boldsymbol{r}_*, t_*) = f_0(t_b) + \varepsilon f_1(t_b) + \varepsilon g_1(t_b) z_b + \phi_{vr}^{new}(\boldsymbol{r}_*) + \phi^{new}(\boldsymbol{r}_*, t_*), \tag{5.6}$$

where $\phi_{vr}^{new}(\boldsymbol{r}_*)$ is the potential due to the vortex ring after the relocation.

5.2. *Modification for toroidal geometry and rejoining*

The numerical transformation of a singly connected bubble to a toroidal one is carried out by removing nodes 1 and $N+1$, corresponding to the impact point. This transform is performed when the distance between two nodes is less than about 0.02 times the equivalent radius of the bubble. The bubble surface and the remnant potential are re-interpolated into its doubly connected shape and re-discretized.

As the bubble evolves in toroidal form, the jet may become very narrow and the bubble has a tendency to rejoin, possibly via evaporation or an instability. Best (1994) and Lee, Klaseboer & Khoo (2007) modelled the rejoining for an axisymmetric bubble, which takes place on the axis of symmetry. In our numerical simulations, the rejoin is performed when the nearest node on the bubble to the axis of symmetry is less than 0.02 times the equivalent radius of the bubble. In the rejoining process, the nearest node and one of its neighbours, either the node above or below it that

is closer to the axis, are placed on the axis of symmetry. The total potential remains constant at these two nodes for such small displacements.

After the bubble rejoins, the vortex ring is removed and its potential is added to the total potential according to (5.2). A doubly connected bubble is now transformed into a singly connected one. The boundary-integral equations are applied identically as was done earlier for the jet impact. Best (1994) and Lee *et al.* (2007) provide further details on the geometrical treatment of the rejoining process.

For the problem under consideration, an axisymmetric MEL is used. However, the principle described here is not limited to axisymmetric configurations, but can also be applied to fully three-dimensional cases (Wang 1998, 2004; Zhang *et al.* 2001).

6. Spherical bubbles in a standing wave

In this section, we will evaluate the present model against the Keller equation for spherical bubbles, identifying the regimes of parametric space where the bubble may be regarded as approximately spherical.

In the calculations to be described in §§ 6 and 7, the parameters for the liquid are chosen at $\rho_\infty = 1000\,\mathrm{kg\,m^{-3}}$, $c_\infty = 1500\,\mathrm{m\,s^{-1}}$ and $p_\infty = p_{atm} = 101.3\,\mathrm{kPa}$, where p_{atm} is the standard atmospheric pressure. The reference velocity U and the bubble-wall Mach number ε are given by $U = \sqrt{p_\infty/\rho_\infty}$ $(= 10\,\mathrm{m\,s^{-1}})$ and $\varepsilon = U/c_\infty (= 1/150)$. We will not consider the effects of vapour pressure in the computation (i.e. $p_v = 0$). The ratio of the specific heats of the gas content is chosen as $\gamma = 1.4$. The surface tension coefficient σ is equal to $0.07\ \mathrm{N\,m^{-1}}$. The initial pressure of the bubble gas is chosen as follows:

$$p_{g0} = p_\infty + 2\sigma/R_0, \tag{6.1}$$

which is consistent with the ambient pressure and surface tension.

Consider a cavitation bubble at an antinode of a standing wave $\theta_0 = \pi$, where the Bjerknes force vanishes and the bubble remains spherical. The acoustic standing wave has amplitude $p_a = 1.2\,\mathrm{atm}$, frequency $f = 26.5\,\mathrm{kHz}$ and the bubble has initial radius $R_0 = 4.5\,\mu\mathrm{m}$. This is a classical SBSL case (Brenner *et al.* 2002). For this case, the acoustic wave frequency f is much smaller than the natural frequency f_n of the bubble, $f = 0.033 f_n$.

As shown in figure 2, the MEL result of the radius history agrees well with the spherical theory based on the Keller equation for seven oscillations. The bubble expands more than five times its ambient radius, and then collapses over a very short period (less than $5\,\mu\mathrm{s}$). This violent collapse causes the adiabatic compression of the bubble gas yielding very high pressures and temperatures, thus providing the physical internal environment for sonoluminescence and sonochemistry. The bubble subsequently vibrates with roughly its natural frequency. The maximum bubble-wall velocity is $27.6\,\mathrm{m\,s^{-1}}$ achieved during the first collapse phase, the corresponding maximum Mach number is 0.018, and therefore the weakly compressible theory should be valid for this case.

Our calculations show that the bubble for this case also remains approximately spherical when it is not initiated at the antinodes. As shown in figure 3(*a*), the bubble initiated at $\theta_0 = \pi/4$, the mean position between the node and antinode of the acoustic pressure field, remains spherical after about five cycles of the incident wave at $26.5\,\mathrm{kHz}$ $(T_a = 3.774\,\mu\mathrm{s})$, which equals 146 cycles of natural oscillation of the bubble $(T = 0.125\,\mu\mathrm{s})$. The computed radius history of the MEL model agrees

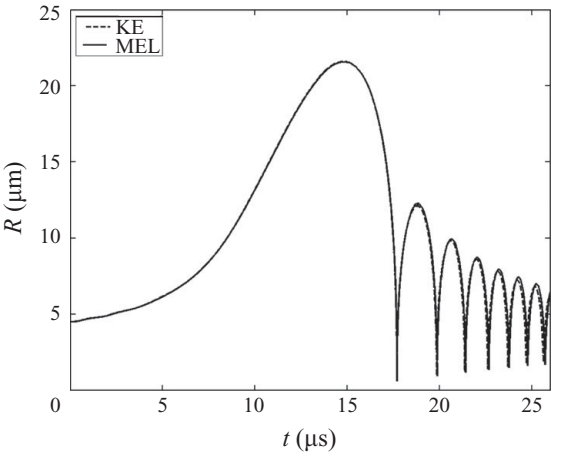

FIGURE 2. Comparison of the radius of a spherical bubble using the Keller equation (KE) and the mixed-Eulerian–Lagrangian method (MEL). The case shows a bubble at an initial radius $R_0 = 4.5\,\mu\text{m}$ and initial pressure $p_{g0} = 1.3\,\text{atm}$ (0.3 atm due to surface tension) in a standing wave having amplitude of pressure $p_a = 1.2\,\text{atm}$ and frequency $f = 26.5\,\text{kHz}$. The bubble is initially located at the antinode of the pressure field $\theta_0 = \pi$.

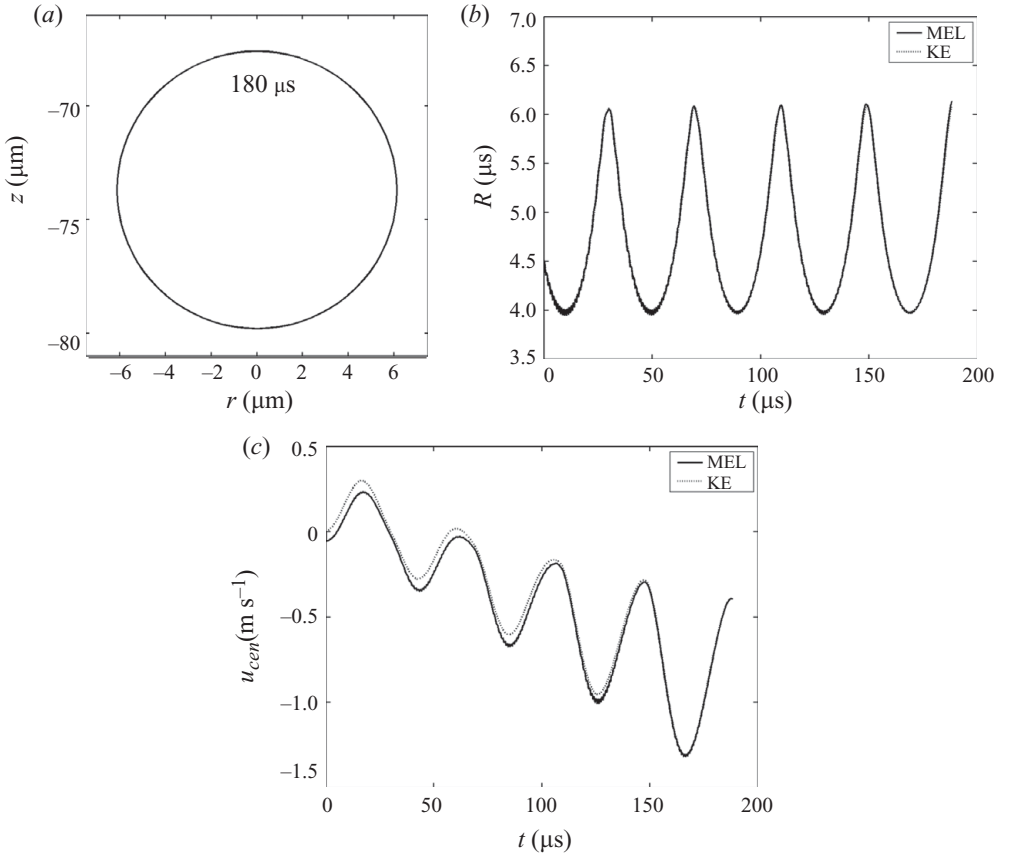

FIGURE 3. (*a*) Bubble shape at the end of the 146 oscillation cycles at $p_a = 1.2\,\text{atm}$, $f = 26.5\,\text{kHz}$, $R_0 = 4.5\,\mu\text{m}$, $p_{g0} = 1.30\,\text{atm}$ and $\theta_0 = \pi/4$. Comparison of the KE and MEL for (*b*) the radius history and (*c*) the moving velocity u_{cen} of the bubble geometrical centre.

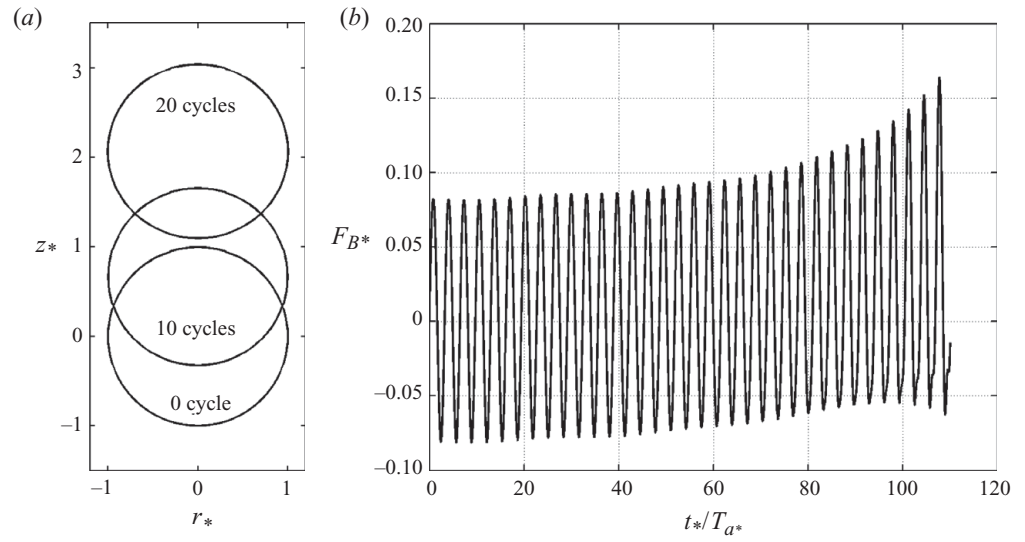

FIGURE 4. (*a*) The bubble shapes initially at the end of 10 and 20 cycles of the acoustic wave for the acoustic bubble characterized by $a_* = 1.5$, $\omega_* = 0.9\omega_{n*}$, $\sigma_* = 0.0691$ and $\theta_0 = \pi/2$; (*b*) the history of the Bjerknes force.

fairly well with that of the spherical theory (figure 3*b*). The bubble oscillates with the acoustic wave, as well as with its natural frequency at much smaller amplitude.

Since the problem considered is axisymmetric, the bubble's displacement has only one component in the z-direction. As shown in figure 3(*c*), the velocity u_{cen} of the bubble centroid (the geometrical centre) along the z-axis reduces with time, vibrating with the driving acoustic wave. It becomes negative at the start of the second collapse phase and the bubble moves towards the antinode at $\theta_0 = 0$. The computed bubble centroid velocity history agrees well with that of the spherical theory (figure 3*c*). However, a small difference is noted during the early stage because the initial value of u_{cen} is set to zero in the spherical bubble theory but is non-zero in the present model. Thus, the bubble motion subjected to a standing wave at low frequency can thus be approximated well by using a spherical bubble model.

7. Bubble behaviour subjected to standing wave at high frequency

Consider the case of a standing wave with the amplitude $p_a = 1.5$ atm and much higher frequency $f = 306.6$ kHz, with the bubble at an initial radius $R_0 = 10\,\mu$m. In this case, the acoustic wave frequency is comparable with the bubble's natural frequency, $f = 0.9 f_n$.

7.1. *The bubble initiated at a node*

At the node where $\theta_0 = \pi/2$, the acoustic pressure vanishes, $p_a = 0$, and the non-spherical Bjerknes force is most prominent, $F_{B*} = \varepsilon V_* \omega_*^2 \sin(\omega_* t_*)$. As shown in figure 4(*a*), the bubble remains near-spherical even after 10 and 20 acoustic cycles of the acoustic wave. The bubble volume does not change significantly since the acoustic pressure vanishes at the node. The bubble moves along the z-axis. As shown in figure 4(*b*), the Bjerknes force vibrates harmonically at approximately constant amplitude and its mean value is positive and increases slightly with time.

Consequently, the accumulated Bjerknes force drives the bubble translation but does not cause non-spherical deformation.

In general, the acoustic pressure has the form

$$p_{a*}(t_*) = a_* \cos(\theta_0) \sin(\omega_* t_* + \theta_1), \tag{7.1}$$

where θ_1 reflects the inception time of the bubble. Our simulations show that the bubble remains spherical at $\theta_1 \neq 0$ but its direction of translation depends on θ_1.

7.2. *The bubble initiated midway between a node and an antinode*

Our calculations have shown that non-spherical effects are most prominent at the mean position between the node and the antinode. At $\theta_0 = \pi/4$ and $3\pi/4$, the bubble initiated midway between the antinode and a node is sketched in figures 5(*a*) and 5(*b*), respectively (the time axis is scaled by the period of the acoustic wave $T_{a*} = 0.328$). At $\theta_0 = \pi/4$, the bubble motion begins with a collapse (figure 5*c*), since the acoustic pressure begins with its positive half-period. While $\theta_0 = 3\pi/4$, the bubble begins with expansion (figure 5*d*) as the acoustic pressure starts with its negative half-period. In both cases, the bubble undergoes about three cycles of oscillation.

At $\theta_0 = \pi/4$, the bubble centroid z_{cen*} migrates in the positive z-direction (figure 5*e*). Its speed generally increases with time, but vibrates up and down associated with the bubble's oscillation. The migration speed of a bubble is inversely proportional to its volume and thus migrates rapidly when it is near its minimum volumes. The Bjerknes force vibrates with the bubble volume with the positive components dominating the behaviour leading to a positive net displacement.

At $\theta_0 = 3\pi/4$, the bubble centroid moves slightly along the z-axis during the first-half cycle, when the Bjerknes force F_{B*} is positive (figure 5*f*). The amplitude of the negative part of the Bjerknes force F_{B*} is slightly larger than the positive part during the first cycle and this difference becomes significant during the later two cycles of oscillation. As a result, the bubble centroid moves in the negative z-direction from the end of the first oscillation.

In the above two cases $\theta_0 = \pi/4$ and $3\pi/4$, the bubble migrates towards the node, which is opposite to the case shown in figure 3, where the bubble migrates to the antinode. This is consistent with the result noted for spherical bubbles: bubbles of sufficiently small radius are drawn towards the antinodes of the standing pressure wave, whereas bubbles of larger radius are attracted to the nodes (Reddy & Szeri 2002). An acoustic standing wave can thus be used to trap a bubble at a particular location despite the influence of buoyancy (Crum 1975; Trinh & Hsu 1986).

In the example considered in figure 6, we not only illustrate the bubble shapes for the examples discussed in figure 5 but also show the influence of changing the equation of state from adiabatic to isothermal. At $\theta_0 = \pi/4$, shown in figure 6(*a–d*), the bubble is approximately spherical shortly before the end of the third collapse (figure 6*a*). At the end of the collapse phase, a jet forms rapidly along the z-axis as a result of the positive Bjerknes force. The Bjerknes force is a non-spherical effect and may result in bubble jetting. The jet impacts the opposite bubble surface and penetrates the bubble, followed by the bubble expanding in toroidal form for a very short period (figure 6*b*). During this process, the liquid jet becomes very thin, and the bubble rejoins near the top of the bubble surface to become a singly connected form again. The subsequent rebounding in singly connected form is shown in figure 6(*c*), returning to a near-spherical shape. The jet first diminishes gradually and then develops an outward protrusion at the end of the expansion phase. This behaviour is due to bubble collapse being driven by the variable pressure of the liquid external to the

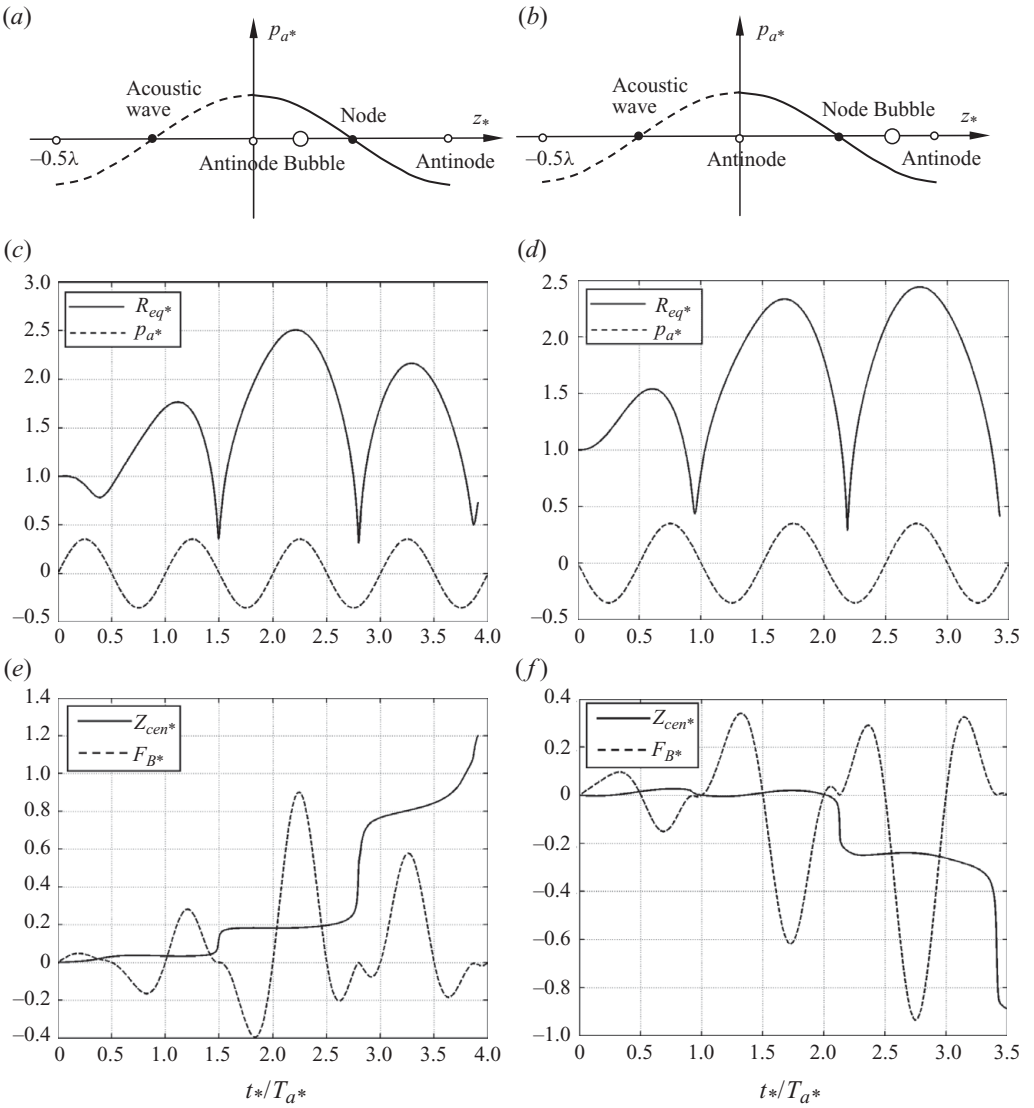

FIGURE 5. Histories of the acoustic bubble characterized by $a_* = 1.5$, $\omega_* = 0.9\omega_{n*}$, $\sigma_* = 0.0691$ and $\theta_0 = \pi/4$ (a,c,d), $\theta_0 = 3\pi/4$ (b,d,f): (a,b) the initial positions of the bubble; (c,d) the bubble equivalent radius R_{eq*} and acoustic pressure at the bubble centre p_{a*}; (e,f) the bubble centroid z_{cen*} and Bjerknes force F_{B*}.

bubble leading to non-spherical shape, whereas bubble expansion is driven by the uniform pressure of the gas inside the bubble leading to a more spherical shape. Similar behaviour is also observed during the next oscillation period. As shown in figure 6(d), a wider jet forms along the z-axis earlier than in the third collapse phase and penetrates the bubble around the end of the collapse phase.

Figure 6(e–h) shows the bubble shapes during similar stages for $\theta_0 = 3\pi/4$, showing the similar dynamic features as in figure 6(a-d) for $\theta_0 = \pi/4$. The bubble remains approximately spherical near the end of the second collapse before forming a jet in the negative z-direction (figure 6e). This jet impacts the opposite bubble surface and

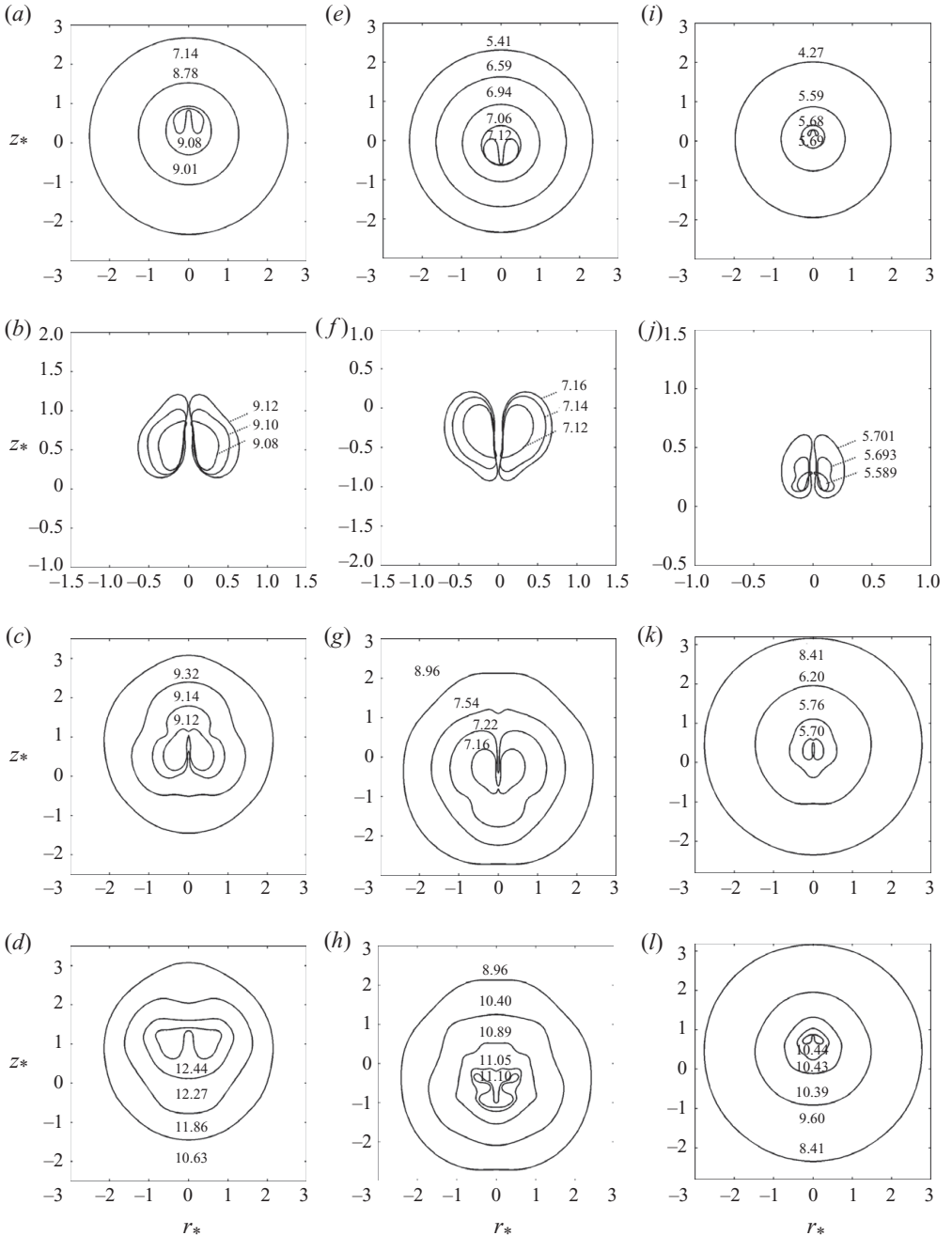

FIGURE 6. Acoustic bubble shapes characterized by $a_* = 1.5$, $\omega_* = 0.9\omega_{n*}$, $\sigma_* = 0.0691$ and $\theta_0 = \pi/4$, $\gamma = 1.4$ (*a–d*), $\theta_0 = 3\pi/4$, $\gamma = 1.4$ (*e–h*) and $\theta_0 = \pi/4$, $\gamma = 1.0$ (*i–l*), during (a, e, i) the last collapse phase in singly connected form, (b, f, j) the first expansion phase in toroidal form, (c, g, k) the further expansion after joined in a singly connected form and (d, h, l) the subsequent collapse phase.

penetrates the bubble around the end of the collapse phase. This is consistent with the negative average Bjerknes force observed in figure 5(*f*). The bubble then expands for a short period in toroidal form (figure 6*f*), before rejoining to form a singly connected

bubble near the bottom. The bubble expands in a singly connected form for most of this expansion period, when the bubble returns to a near-spherical shape. The bubble further undergoes its third collapse phase (figure 6*g*), when a downward jet forms earlier than in the second collapse phase. The jet impacts occur at slightly different times, being on the opposite side of the node to the example considered in figure 5, with the centroid motion and Bjerknes force being nearly opposite to each other, only the initial stage leading to a slight difference.

For the above two cases, our simulations show that detailed results depend on its inception phase θ_1; however, the bubble deforms in a similar way as that at $\theta_1 = 0$, in particular, the jet and translation of the bubble are both towards the node.

7.3. *The isothermal case*

Heat and mass transfers take place across the bubble surface. Although some models code in a change from isothermal to adiabatic when the bubble radius reaches equilibrium radius or a smaller radius (Szeri *et al.* 2003; Coussis & Roy 2008), we consider the two limits namely isothermal and adiabatic as the two extreme cases. In the isothermal case, the motion of the bubble is much slower compared to heat and mass transfer, where heat transfer maintains the bubble interior at uniform temperature T_∞, in thermal equilibrium with the surrounding fluid. In the adiabatic case, the bubble motion is much faster so that mass and thermal transfer may be neglected. We have used polytropic exponent $\gamma = 1.0$ for isothermal cases and $\gamma = 1.4$ for adiabatic cases.

With the adiabatic cases considered above (entirely fast mode), we recalculate the case shown in figure 6(*a–d*) with $\gamma = 1.0$, the isothermal case. Figure 6(*i–l*) shows the bubble shapes during the various stages, showing similar dynamic features as in figure 6(*a–d*). The bubble loses its spherical shape at the end of the second collapse phase (figure 6*i*). An upward liquid bubble jet forms, impacting the opposite bubble surface to form a toroidal bubble. The bubble reaches a very much smaller minimum volume with a smaller jet formed, compared to the example in figure 6(*a–d*). The bubble first rebounds in a toroidal form but recombines to a singly connected bubble, expanding continuously and gradually returning to a near-spherical shape (figures 6*j* and 6*k*). These processes are repeated in the next oscillation (figure 6*l*). While this purely isothermal model (entirely slow mode) is unlikely to be appropriate near minimum volume, it shows that the much reduced final volume on rebound leads to an almost spherical bubble.

Figure 7 compares histories of the equivalent bubble radius and the jet velocity for the cases shown in figures 6(*a–d*) and 6(*i–l*) for $\gamma = 1.4$ and 1.0, respectively. The oscillation period and amplitude for $\gamma = 1.0$ has increased. The minimum equivalent radius at $\gamma = 1.0$ and 1.4 is 0.10 and 0.31, respectively. The maximum equivalent radius is 2.8 and 2.5, and the jet velocity is 480 and 270 m s^{-1}, respectively. The slower dynamic case has smaller minimum volume, larger maximum volume, smaller jet but higher jet velocity.

7.4. *Verifications of weak compressibility and convergence to mesh size*

To check the validity of the assumption of the weak compressibility, figure 8 shows the transient bubble-wall Mach number at the jet tip and the average bubble-wall Mach number defined as

$$M_{maen} = \frac{1}{N_1}\sum_{i=1}^{N_1} M_i = \frac{1}{c_\infty N_1}\sum_{i=1}^{N_1}\left|\frac{\partial \varphi}{\partial n}\right|. \tag{7.2}$$

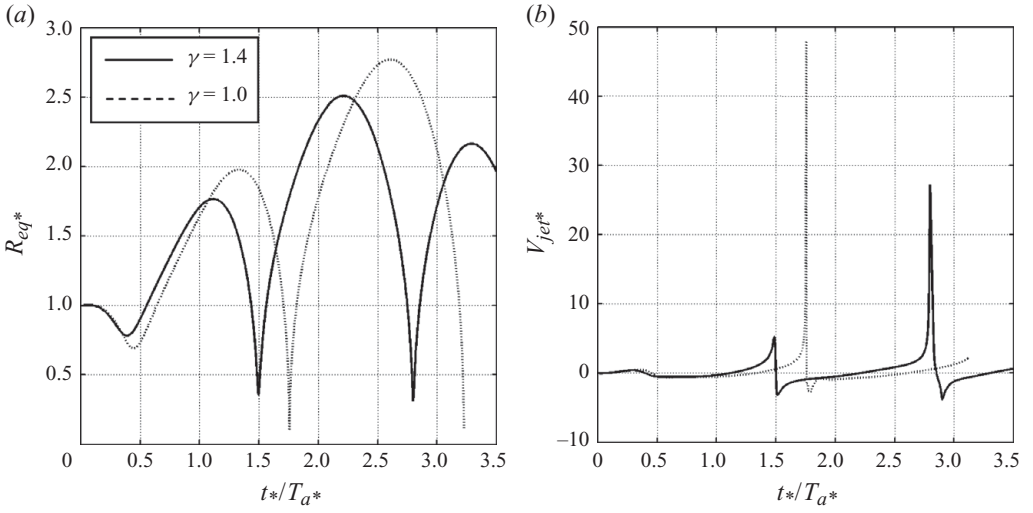

FIGURE 7. Comparison of histories of (*a*) the equivalent bubble radius and (*b*) the jet velocity for the cases shown in figure 6 for $\gamma = 1.0$ and 1.4, respectively.

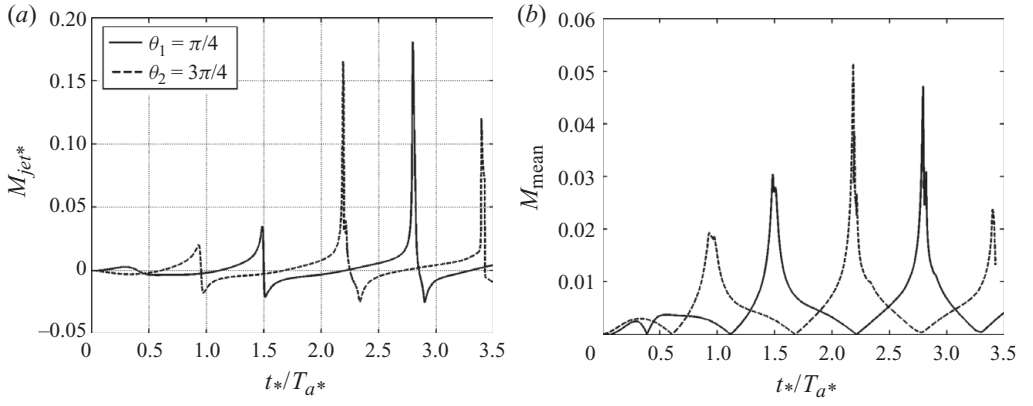

FIGURE 8. The histories of (*a*) the Mach number of the jet M_{jet} and (*b*) the average Mach number M_{mean} for the acoustic bubble characterized by $a_* = 1.5$, $\omega_* = 0.9\omega_{n*}$, $\sigma_* = 0.0691$ and for $\gamma = 1.4$ and $\theta_0 = \pi/4$, $3\pi/4$, respectively.

The cases are at $\theta_0 = \pi/4$, $3\pi/4$ and $\gamma = 1.4$ shown in figures 6(*a–d*) and 6(*e–h*). The maximum jet Mach numbers are 0.18 and 0.165 at $\theta_0 = \pi/4$ and $3\pi/4$ respectively, and it is larger than 0.1 for about 1 % of the bubble lifetime. The maximum average Mach number is close to 0.05 for both cases. Consequently, the weakly compressible model is appropriate for the example considered. The maximum dimensional jet velocities are 270 and 250 m s^{-1}, respectively. This high-speed jetting phenomenon may be the mechanism for releasing the reagents carried in bubbles in the therapeutic application of ultrasound.

Figure 9 shows the comparison of the bubble shapes for the case at $\theta_0 = \pi/4$ and $\gamma = 1.4$ shown in figure 6(*a–d*) at the mesh size $n_1 = 51, 61$ and 71 at (*a*) the first jet impact and (*b*) the second jet impact, respectively. At first jet impact (figure 9*a*), the jet shapes are almost the same. At second jet impact (figure 9*b*), the shapes are

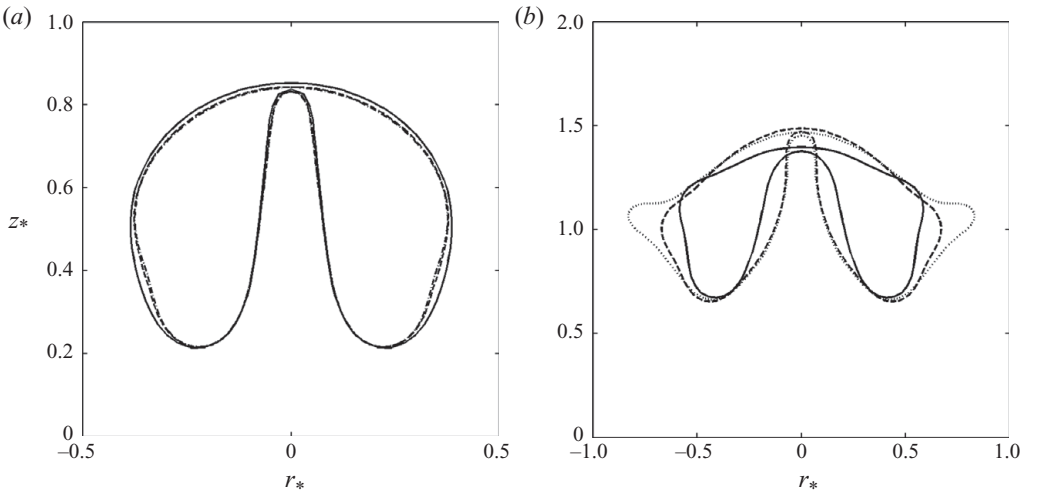

FIGURE 9. The comparison of the bubble shapes for the same case as in figure 6 for $\gamma = 1.4$ and $\theta_0 = \pi/4$ at the mesh size $n_1 = 51$ (——), 61 (----) and 71 (····) at (*a*) the first jet impact at $t_* = 9.010$ and (*b*) the second jet impact at $t_* = 12.48, 12.36, 12.23$, respectively.

slightly different everywhere except at the lateral edges of the bubble; further studies are needed to understand the details of the bubble shape in this instance.

The jetting phenomenon may be relevant to the following medical application. Injected bubbles are often used to carry reagents to the site of a tumour (Kawabata & Umemura 1996) or a blood clot (Wu *et al.* 1988). Once they reach their target, the bubbles are acoustically excited to collapse violently. The jet impact and formation of toroidal bubble will release reagents transported within the bubble that can combat the tumour or clot. In microvessels, dilatation, invagination and rupture are associated with bubble jetting and highly non-spherical bubble shapes (Chen, Brayman & Matula 2008).

7.5. *Summary and conclusions*

A weakly compressible theory for micro-bubble dynamics in an acoustic standing wave is developed using the method of matched asymptotic expansions. The perturbation is performed to second-order in terms of the bubble-wall Mach number. The inner flow for the first two orders near the bubble can be approximated as incompressible. The outer flow for the first two orders far away from the bubble can be described by the linear wave equation and is shown as a direct problem. Thus, the non-spherical bubble dynamics in a weakly compressible liquid is modelled approximately by Laplace's equation with compressible effects appearing only in the far-field condition. A modified boundary-integral formulation is developed based on the weakly compressible theory developed in the paper, which provides physical insight into the phenomena together with computational efficiency.

The boundary-integral model is evaluated against the spherical theory; excellent agreement is obtained with the spherical model for the bubble radius evolution over many oscillations.

We further carried out simulations for non-spherical bubble dynamics. The computation traces jet impact, the transition of the bubble from a singly connected to a doubly connected form, and the recombining of a doubly connected to a singly connected form, and further transitions. The principal conclusions of this study for

a highly non-spherical cavitation bubble in a compressible liquid in a standing wave may be summarized as follows.

(i) The Bjerknes force associated with the acoustic wave leads to a non-spherical effect, which is proportional to the square of the frequency of the acoustic wave. This leads to both the bubble's translation and non-spherical deformation.

(ii) When the acoustic wave frequency is small, the bubble remains approximately spherical in the whole flow field, with spherical theory providing a good approximation. The bubble migrates to the antinode of the acoustic pressure field.

(iii) When the acoustic wave frequency is not small, the bubble remains spherical at the antinode of the acoustic pressure field where the Bjerknes force vanishes. The bubble remains spherical at the nodes, where the Bjerknes force vibrates harmonically at nearly constant amplitude.

(iv) A bubble initiated between the node and antinode may lose its spherical shape at the end of a collapse phase after only a few cycles of oscillations. A high-speed liquid bubble jet forms, impacting the opposite bubble surface and penetrating through the bubble. The bubble first rebounds in a toroidal form but recombines to a singly connected form shortly thereafter. It then expands continuously, gradually returning to its spherical shape. The above phenomenon repeats itself in the next oscillation. The jet and the migration of the bubble are towards the pressure node.

The generic theoretical and computational results developed in this paper for highly non-spherical bubble behaviour in an acoustic standing wave reveal a number of new phenomena that need to be investigated experimentally for a range of special cases that cover studies in sonochemistry, multi-bubble sonoluminescence (MBSL) and SBSL and for extension to closed flows in arteries, arterioles, veins and venules. Physically, more detailed studies for heat and mass transfer at the bubble surface, chemical reactions and viscous effects will be required to evaluate the efficacy of this approach for particular applications.

REFERENCES

Batchelor, G. K. 1968 *An Introduction to Fluid Dynamics*. Cambridge University Press.

Best, J. P. 1993 The formation of toroidal bubbles upon collapse of transient cavities. *J. Fluid Mech.* **251**, 79–107.

Best, J. P. 1994 The rebound of toroidal bubbles. In *Bubble Dynamics and Interface Phenomena* (ed. J. R. Blake, J. M. Boulton-Stone & N. H. Thomas), pp. 405–412. Kluwer.

Blake, J. R., Keen, G. S., Tong, R. P. & Wilson, M. 1999 Acoustic cavitation: the fluid dynamics of non-spherical bubbles. *Phil. Trans. R. Soc.* A **357**, 251–267.

Blake, J. R., Taib, B. B. & Doherty, G. 1986 Transient cavities near boundaries. Part 1. Rigid boundary. *J. Fluid Mech.* **170**, 479–497.

Boulton-Stone, J. M. & Blake, J. R. 1993 Gas bubbles bursting at a free surface. **254**, 437–466.

Brennen, C. E. 1995 *Cavitation and Bubble Dynamics*. Oxford University Press (available online).

Brenner, M. P., Hilgenfeldt, S. & Lohse, D. 2002 Single-bubble sonoluminescence. *Rev. Mod. Phys.* **74**, 425–484.

Brenner, M. P., Lohse, D. & Dupont, T. F. 1995 Bubble Shape Oscillations and the Onset of Sonoluminescence. *Phys. Rev. Lett.* **75**, 954–957.

Calvisi, M. L., Iloreta, J. I. & Szeri, A. J. 2008 Dynamics of bubbles near a rigid surface subjected to a lithotripter shock wave. Part 2. Reflected shock intensifies non-spherical cavitation collapse. *J. Fluid Mech.* **616**, 63–97.

Calvisi, M. L., Lindau, O., Blake J. R. & Szeri, A. J. 2007 Shape stability and violent collapse of microbubbles in acoustic traveling waves. *Phys. Fluids* **19** (4), 047101.

Chen, H., Brayman, A. A. & Matula, T. J. 2008 Microbubble dynamics in microvessels: Observations of microvessel dilation, invagination and rupture. *IEEE Ultrason. Symp.* **1–4**, 1163–1166.

Cole, R. H. 1948 *Underwater Explosions*. Princeton University Press.

Coussis, C. C. & Roy, R. A. 2008 Applications of Acoustics and Cavitation to Noninvasive Therapy and Drug Delivery. *Annu. Rev. Fluid Mech.* **40**, 395–420.

Crum, L. A. 1975 Bjerknes forces on bubbles in a stationary sound field. *J. Acoust. Soc. Am.* **57**, 1363–1370.

Crum, L. A. & Cordry, S. 1994 Single bubble sonoluminescence. In *Bubble Dynamics and Interface Phenomena* (ed. J. R. Blake, J. M. Boulton-Stone & N. H. Thomas), pp. 287–297. Kluwer.

Dahnke, S., Swamy, K. & Keil, F. J. 1999 Modeling of three dimensional pressure fields in sonochemical reactors with an inhomogeneous density distribution of cavitation bubbles. comparison of theoretical and experimental results. *Ultrason. Sonochem.* **6**, 31–41.

Day, C. 2005 Targeted ultrasound mediates the delivery of therapeutic genes to heart muscle. *Phys. Today* **58** (12).

Feng, Z. C. & Leal, L. G. 1997 Nonlinear bubble dynamics. *Annu. Rev. Fluid Mech.* **29**, 201–243.

Eller, A. 1968 Force on a bubble in a standing acoustic wave. *J. Acoust. Soc. Am.* **43** (1), 170–171.

Epstein, D. & Keller, J. B. 1971 Expansion and contraction of planar, cylindrical, and spherical underwater gas bubbles. *J. Acoust. Soc. Am.* **52**, 977–980.

Gilmore, F. R. 1952 The growth or collapse of a spherical bubble in a viscous compressible liquid. *Report No* 26-4, Hydrodynamics Laboratory, California Institute of Technology, Pasadena, California, USA.

Goldberg, B. B., Liu, J.-B. & F. Forsberg 1994 Ultrasound contrast agents – a review. *Ultrasound. Med. Biol.* **20**, 319–333.

Herring, C. 1941 The theory of the pulsations of the gas bubbles produced by an underwater explosion. *US Nat. Defence Res. Comm. Report*.

Hilgenfeldt, S., Brenner, M. P., Grossmann, S. & Lohse, D. 1998 Analysis of Rayleigh–Plesset dynamics for sonoluminescing bubbles. *J. Fluid Mech.* **365**, 171.

Hua, J. & Lou, J. 2007 Numerical simulation of bubble rising in viscous liquid. *J. Comput. Phys.* **222** (2), 769–795.

Johnsen, E. & Colonius, T. 2008 Shock-induced collapse of a gas bubble in shockwave lithotripsy. *J. Acoust. Soc. Am.* **124**, 2011–2020.

Johnsen, E. & Colonius, T. 2009 Numerical simulations of non-spherical bubble collapse. *J. Fluid Mech.* **629**, 231–262.

Kamath, V., Prosperetti, A. & Egolfopoulos, F. N. 1993 A theoretical study of sonoluminescence. *J. Acoust. Soc. Am.* **94**, 248–260.

Kawabata, K. & Umemura, S. 1996 Effect of second-harmonic superimposition on efficient induction of sonochemical effect. *Ultrason. Sonochem.* **3**, 1–5.

Keller, J. B. & Kolodner, I. I. 1956 Damping of underwater explosion bubble oscillations. *J. Appl. Phys.* **27** (10), 1152–1161.

Keller, J. B. & Miksis, M. J. 1980 Bubble oscillations of large amplitude. *J. Acoust. Soc. Am.* **68**, 628–633.

Klaseboer, E., Turangan, C. K., Khoo, B. C., Szeri, A. J., Calvisi, M. L., Sankin G. N. & Zhong, P. 2007 Interaction of lithotripter shockwaves with single inertial cavitation bubbles. *J. Fluid Mech.* **593**, 33–56.

Lauterborn, W. & Kurz, T. 2010 Physics of bubble oscillations. *Rep. Prog. Phys.* **73**, 106501.

Lee, M., Klaseboer, E. & Khoo B. C. 2007 On the boundary integral method for the rebounding bubble. *J. Fluid Mech.* **570**, 407–429.

Leighton, T. 1994 *The Acoustic Bubble*. Academic Press.

Lezzi, A. & Prosperetti, A. 1987 Bubble dynamics in a compressible liquid. Part. 2. Second-order theory. *J. Fluid Mech.* **185**, 289–321.

Lundgren, T. S. & Mansour, N. N. 1991 Vortex ring bubbles. *J. Fluid Mech.* **72**, 391–399.

Matula, T. J. Cordry, S. M., Roy, R. A. & Crum, L. A. 1997 Bjerknes force and bubble levitation under single-bubble sonoluminescence conditions. *J. Acoust. Soc. Am.* **102** (3), 1522–1527.

Miksis, J. M., Vanden-Broeck, J. M. & Keller, J. B. 1982 Rising bubbles. *J. Fluid Mech.* **123**, 31–41.

Moore, D. W. 1963 The boundary layer on a spherical gas bubble. *J. Fluid Mech.* **16**, 161–176.

Pedley, T. J. 1968 The toroidal bubble. *J. Fluid Mech.* **32**, 97–112.

Popinet, S. & Zaleski, S. 2002 Bubble collapse near a solid boundary: a numerical study of the influence of viscosity. *J. Fluid Mech.* **464**, 137–163.

Prosperetti, A. 1977 Viscous effects on perturbed spherical flows. *Q. Appl. Math.* **34**, 339–352.

Prosperetti A., Crum, L. A. & Commander, K. W. 1988 Nonlinear bubble dynamics. *J. Acoust. Soc. Am.* **83**, 502–514.

Prosperetti, A. & Lezzi, A. 1986 Bubble dynamics in a compressible liquid. Part 1. First-order theory. *J. Fluid Mech.* **168**, 457–478.

Putterman, S. J. & Weninger, K. R. 2000 Sonoluminescence: how bubbles turn sound into light. *Annu. Rev. Fluid Mech.* **32**, 445–476.

Reddy, A. J. & Szeri, A. J. 2002 Coupled dynamics of translation and collapse of acoustically driven microbubbles. *J. Acoust. Soc. Am.* **112** (4), 1346–1352.

Szeri, A. J., Storey, B. D., Pearson, A. & Blake, J. R. 2003 Heat and mass transfer during the violent collapse of nonspherical bubbles. *Phys. Fluids* **15**, 2576–2586.

Trinh, E. H. & Hsu, C.-J. 1986 Equilibrium shapes of acoustically levitated drops. *J. Acoust. Soc. Am.* **79**, 1335–1338.

Turangan, C. K., Jamaluddin, A. R., Ball, G. J. & Leighton, T. G. 2008 Free-Lagrange simulations of the expansion and jetting collapse of air bubbles in water. *J. Fluid Mech.* **598**, 1–25.

Van Dyke, M. D. 1975 *Perturbation Methods in Fluid Mechanics*, 2nd edn. Parabolic Press.

Versluis, M., Goertz, D. E., Palanchon, P., Heitman, I. L., van der Meer, S. M., Dollet, B., Jong, N. D. & Lohse, D. 2010 Microbubble shape oscillations excited through ultrasonic parametric driving. *Phys. Rev.* E **82**, 026321.

Wang, Q. X. 1998 The numerical analyses of the evolution of a gas bubble near an inclined wall. *Theor. Comput. Fluid Dyn.* **12**, 29–51.

Wang, Q. X. 2004 Numerical modelling of violent bubble motion. *Phys. Fluids* **16** (5), 1610–1619.

Wang, Q. X. & Blake, J. R. 2010 Non-spherical bubble dynamics in a compressible liquid. Part 1. Travelling acoustic wave. *J. Fluid Mech.* **659**, 191–224.

Wang, Q. X., Yeo, K. S., Khoo, B. C. & Lam, K. Y. 1996*a* Nonlinear interaction between gas bubble and free surface. *Comput. Fluids* **25** (7), 607.

Wang, Q. X., Yeo, K. S., Khoo, B. C. & Lam, K. Y. 1996*b* Strong interaction between buoyancy bubble and free surface. *Theor. Comput. Fluid Dyn.* **8**, 73.

Wang, Q. X., Yeo, K. S., Khoo, B. C. & Lam, K. Y. 2005 Vortex ring modelling for toroidal bubbles. *Theor. Comput. Fluid Dyn.* **19** (5), 303–317.

Wu, Y., Unger, E. C. McCreery, T. P., Sweitzer, R. H., Shen, D., Wu, G. & Vielhauer, M. D. 1988 Binding and lysing of blood clots using MRX-408. *Invest. Radiol.* **33**, 880–885.

Young, F. R. 1989 *Cavitation.* McGraw-Hill.

Yue, P., Feng, J. J., Bertelo, C. A. & Hu, H. H. 2007 An arbitrary Lagrangian–Eulerian method for simulating bubble growth in polymer foaming. *J. Comput. Phys.* **226** (2), 2229–2249.

Zhang, S. G. & Duncan, J. H. 1994 On the non-spherical collapse and rebound of a cavitation bubble. *Phys. Fluids* **6** (7), 2352–2362.

Zhang, S. G., Duncan, J. H. & Chahine, G. L. 1993 The final stage of the collapse of a cavitation bubble near a rigid wall. *J. Fluid Mech.* **257**, 147–181.

Zhang, Y. L., Yeo, K. S., Khoo, B. C. & Wang, C. 2001 3D jet impact and toroidal bubbles. *J. Comput. Phys.* **166**, 336–360.